Controlling the Dominant Length Scale of Liquid–Liquid Phase Separation in Spin-coated Organic Semiconductor Films

*Jacobus J. van Franeker, Daniel Westhoff, Mathieu Turbiez, Martijn M. Wienk, Volker Schmidt, and René A. J. Janssen**

Organic electronic devices are often made by solution processing a multi-component ink. During solution processing, for example, via spin coating, the solvent evaporates and the solid components deposit on the substrate. The morphology of this layer can range from well-mixed to extensively phase separated. To optimize device performance, it is essential to control the degree and dominant length scale of phase separation. Currently, the mechanism of phase separation induced by solvent evaporation is poorly understood. It has been shown that length scales are influenced by spin speed, drying time, final layer thickness and the ratio between the solid components, but a complete experimental dataset and consistent theoretical understanding are lacking. In this contribution, in situ measurements during spin coating and a simple numerical model are used to understand the drying process. In addition, an advanced image analysis of transmission electron micrographs of films processed under a wide range of processing conditions is carried out. A normalized drying rate is proposed as the key parameter that controls the dominant length scale of phase separation.

1. Introduction

One of the main advantages of organic electronic devices is the ability to use solution processing in their assembly. Solution processing can be applied cost-effectively on large areas using coating and printing methods. Virtually all modern organic electronic devices consist of multiple solid components which are deposited from one or more solvents. During the evaporation of these solvents a certain morphology is formed by the solid components, which can either remain well-mixed or form a well phase-separated morphology. Either of which can be desired, depending on the required device functionality. In organic light-emitting devices the dye has to be well-mixed into the host matrix.[1] In organic solar cells, some degree of phase separation between donor polymer and acceptor fullerene is required to form continuous phases, but optimal length scales are limited by the exciton diffusion length, which is of the order of 10 nm.[2] Finally, for organic ferroelectric resistive switches phase separation has to form columns of a polymer semiconductor inside a ferroelectric polymer matrix through the entire film thickness.[3] Also, in other solution processed materials, phase separation can be a desired effect, for example in the fabrication of core-shell particles,[4] microporous membranes,[5] and ordered colloidal droplets.[6]

Phase separation induced by a temperature quench is relatively well studied and understood.[7] Here, both early-stage processes (spinodal demixing) and late-stage processes (coarsening) can influence the final morphology. In the formation of thin films by solution processing, concentration-quench-induced phase separation can occur at a constant temperature due to solvent evaporation. The final thin-film morphology is the result of a complex combination of processes: apart from the early and late-stage liquid–liquid phase separation, gelation, and solidification can also play a role in effectively freezing a non-equilibrium morphology.

To be able to quantitatively discuss typical size distributions in phase-separated films, we will define a dominant length scale in Section 2.1. Later, we will show that this dominant length scale scales with an average equivalent radius of droplets in phase-separated morphologies. Because of this relation, the term "length scales" is used generic and can be used for both definitions. Length scales in phase-separated films, which are spin coated from three-component inks (a solvent and two solid components), are commonly thought to depend on either the drying rate or time (mainly controlled by the spin speed ω and the choice of solvent),[8,9] or on the final thickness (influenced by ω and the initial concentration C).[10] In this contribution we

J. J. van Franeker, Dr. M. M. Wienk, Prof. R. A. J. Janssen
Molecular Materials and Nanosystems &
Institute for Complex Molecular Systems
Eindhoven University of Technology
P.O. Box 513, 5600 MB, Eindhoven, The Netherlands
E-mail: r.a.j.janssen@tue.nl
J. J. van Franeker
Dutch Polymer Institute (DPI)
P.O. Box 902, 5600, AX, Eindhoven, The Netherlands
D. Westhoff, Prof. V. Schmidt
Institute of Stochastics
Ulm University
D-89069, Ulm, Germany
Dr. M. Turbiez
BASF Schweiz AG
Schwarzwaldallee 215, CH-4002, Basel, Switzerland

DOI: 10.1002/adfm.201403392

ADVANCED FUNCTIONAL MATERIALS
www.afm-journal.de

show that these dependencies are only valid for a constant initial concentration C or a constant spin speed ω, respectively.

The main focus in this contribution is on thin-films for organic solar cells, which are made by spin coating a three-component ink: a semiconducting polymer is mixed with a fullerene derivative in a common solvent. In many un-optimized photoactive layers, fullerene domains are formed inside a polymer matrix with diameters up to a few hundred of nanometers. These droplet-like fullerene domains originate from liquid–liquid phase separation.[9,11] The relation between the morphology and device performance of solar cells with droplet-like fullerene-rich domains in a mixed polymer-fullerene matrix has been subject of several studies.[9,12–14] The studies reveal that the droplet morphology is generally not beneficial to device performance: efficient solar cells require smaller length scales. Thin films with smaller length scales are commonly made by adding an extra solvent and thus processing from a four-component ink.[15]

Although these droplet-like morphologies are not directly relevant to high-performing solar cells, the relevance of these three-component inks is twofold. Firstly, we are currently far from understanding the complex processes that determine the length scales when processing four-component inks to an optimized solar cell. The increased understanding of three-component inks is a step towards that goal and here we address the relation between processing and morphology. Secondly, length scales in these droplet-like morphologies are important for other applications, for example the organic ferroelectric resistive switches or the fabrication of microporous membranes. For this reason, in this contribution we investigate the key parameters that control the dominant length scale in blend films, formed by phase separation of three-component mixtures. Late-stage Ostwald ripening[16] is a possible origin of the experimentally observed dependency of these length scales on drying time.[9] However, it is expected that the amplification of a characteristic length scale in the early-stage spinodal demixing process can also contribute to length scales in the dry blend films.[7]

We use in situ measurements to study the kinetics of film formation from three-component inks to obtain real-time information on layer thickness and phase separation during spin coating. A relatively simple model is used to understand these drying curves. This is combined with advanced image analysis of transmission electron micrographs of dry films. We find that the dominant length scale of phase separation scales with a normalized drying rate over two orders of magnitude. We show that this scaling of dominant length scale to normalized drying rate can originate both from a dependency of length scales on quench rate in early stage spinodal demixing as well as from a dependency of length scales on coarsening time in late-stage ripening processes.

2. Results

2.1. Combined In Situ Monitored Drying and Length Scale Analysis

Several optical in situ techniques exist to monitor film formation during spin coating.[17] We use laser-based interference measurements to determine the thickness of the wet layer during spin coating. Due to solvent evaporation, repetitive interference maxima and minima occur when the layer thickness matches conditions for constructive and destructive thin-film interference, respectively. Then, using the final layer thickness of the dried film (h_{dry}), which is independently measured with a profilometer, the wet-layer thickness development can be back-calculated. In addition, after the onset of liquid–liquid phase separation scattered light can be detected, due to the difference in refractive index of both phases (**Figure 1**a). This combination allows us to determine the concentration at the onset of phase separation, as well as the rate of solvent evaporation, as shown in the Supporting Information. These measurements are always done on the center of rotation to minimize disturbances and to avoid positional effects on the measured evaporation rate.

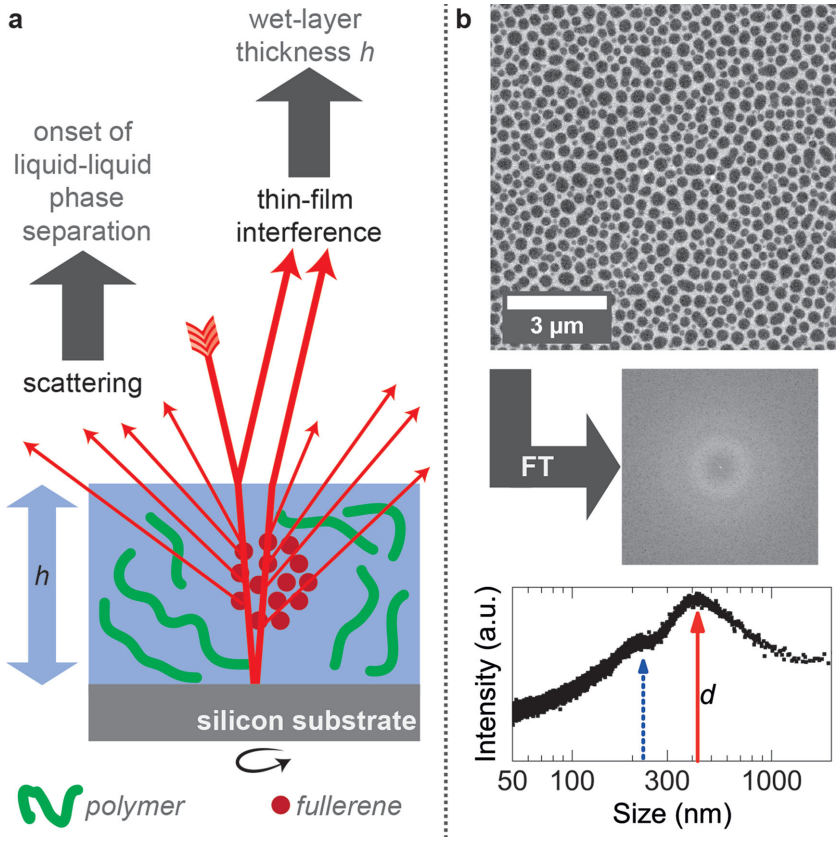

Figure 1. a) The setup is schematically shown in panel. A slightly defocused laser beam is incident on the spinning substrate and during solvent evaporation the interference and scattering signals are collected by two separate photodiodes positioned under specular and off-specular angles. The schematic in (b) shows how dry films are analyzed by low-magnification TEM. At least five images per sample are Fourier transformed (FT), radially integrated, and averaged. Inverting the *x*-axis to real-space coordinates reveals a main peak, which indicates dominant length scale *d* (solid red arrow) and a smaller peak or shoulder at smaller distances (dotted blue arrow).

The interference experiments are performed on silicon substrates coated with a layer of PEDOT:PSS, which allows the dry films to be detached by floating on water and subsequently analyzed by transmission electron microscopy (TEM). The TEM-samples are taken from the approximate location of the in situ measurements. We note that the dry-layer morphologies as seen by TEM do not necessarily correspond to the on-set or any other intermediate stage of the phase separation process. The purpose of this study is to relate final layer morphology to in situ processing conditions.

We mainly focus on the combination of a diketopyrrolopyrrole-quinquethiophene copolymer (PDPP5T) with a fullerene derivative ([6,6]-phenyl-C_{71}-butyric acid methyl ester, [70]PCBM) (structures are shown in the Supporting Information, Figure S1) in a 1:2 weight ratio dissolved in chloroform. This weight ratio was chosen because it provides optimized solar cell performance when PDPP5T and [70]PCBM are spin coated or doctor bladed from chloroform with *o*-dichlorobenzene (oDCB) as co-solvent. The corresponding current density – voltage characteristics and TEM images for films spin coated from chloroform without and with oDCB are shown in Figure S2 and reveal that processing from four-component mixtures results a much smaller phase separation and correspondingly higher performance. As explained in the introduction, the purpose of this paper is to understand the parameters that control morphology formation and –as first step– we focus on films cast from chloroform only.

The TEM image in Figure 1b obtained when spin coating PDPP5T and [70]PCBM from chloroform shows a high contrast between droplets and continuous matrix. The droplet phase is consists of almost pure [70]PCBM, while the matrix is rich in PDPP5T with admixed [70]PCBM.[9] The contrast in the TEM originates from both the electron density difference between polymer and [70]PCBM and the height difference between droplet and matrix. This is caused by the different amounts of solvent present in the two liquid phases that form during drying and causes the [70]PCBM droplets to stick out of the dry film.[9] A dominant length scale in these images can be determined by 2D Fourier-transformations (FT) of the TEM images, as is shown in Figure 1b. The radially integrated FT exhibit a characteristic main peak. We define the position of this peak as a dominant length scale d. Later we will show that d is related with the average distance between the droplet midpoints.

2.2. Spin Coating Model

During spin coating two main time regimes can be distinguished. Initially rotation causes a radially outward flow of material. The second regime is solvent evaporation. Both regimes are well described by differential equations. The flow regime—assuming an initially uniform layer—is described by Equation 1, which was derived by Emslie et al.:[18]

$$\frac{\mathrm{d}h}{\mathrm{d}t} = -2\frac{\rho\omega^2}{3\eta}h^3 \tag{1}$$

Here, ρ is the density of the ink and η is the viscosity of the ink. The equation shows that the rate of thickness change ($\mathrm{d}h/\mathrm{d}t$) is proportional to the current thickness ($h = h[t]$) to the third power. This means the thickness decreases rapidly in the first phase of spin coating but that causes the thinning rate to decrease very rapidly in time.

Evaporation can be described by mass-transfer coefficients as shown by Bornside et al.[19] The thinning rate caused by solvent evaporation is given by:

$$\frac{\mathrm{d}h}{\mathrm{d}t} = -\phi\frac{cD_\mathrm{g}p_\mathrm{vp}M}{\sqrt{\nu_g}\rho RT}\sqrt{w} \tag{2}$$

Here M, p_vp, and ρ are the molar mass, the vapor pressure, and the density of the solvent, respectively. The constant c is taken from Bornside et al.[19] The binary diffusion coefficient of the solvent in the overlying gas is denoted as D_g and the kinematic viscosity of the overlying gas as ν_g. Finally, R is the ideal gas constant and T the temperature. Except for the final part of solvent evaporation, where the solvent volume fraction ϕ is of influence, this thinning rate is constant. Thus, as soon as thinning due to solvent evaporation is sufficiently larger than the thinning due to flow, we expect the thickness to decrease linearly over time.

Equations 1 and 2 are coupled and solved numerically using the NDSolve function in Wolfram Mathematica 9.0. All input parameters except the ink viscosity are known or can be estimated (see Supporting Information for full details). For fast drying solvents, it can occur that all solvent has evaporated before the spin coater had reached the set spin speed. Thus, it proved to be essential to include spin speed acceleration in the model. Considering that there are no fit parameters, **Figure 2**a shows that the model (thin solid lines) describes the measurements (squares) well for a wide range of spin speeds and concentrations. The two expected regimes can be seen: first rapid thinning due to flow, followed by a linear decrease in thickness due to evaporation.

2.3. Phase Separation

For PDPP5T and [70]PCBM, phase separation always occurs in the "evaporation" regime where the thinning rate is constant as is shown by the pink circles in Figure 2. Because phase separation occurs after flow has ceased, we do not detect any effect of shear forces in dry-layer morphologies. This is relevant for the applicability of our results to other coating processes. In fact, the performance of PDPP5T:[70]PCBM solar cells is very similar for spin coated and doctor bladed films (Figure S2, Supporting Information) from chloroform. Hence, we expect that our analysis is applicable to a wider range of coating techniques.

The average solvent concentration at which phase separation occurs is 80% (see Supporting Information). The assumption to use an average concentration is of course only justified if solvent evaporation from the air-exposed surface is slower than solvent diffusion *to* that surface. If the opposite was true, the surface layer would be depleted of solvent and thus phase separation would initiate at the surface. The fact that the (bulk) concentration at which the onset phase separation occurs is

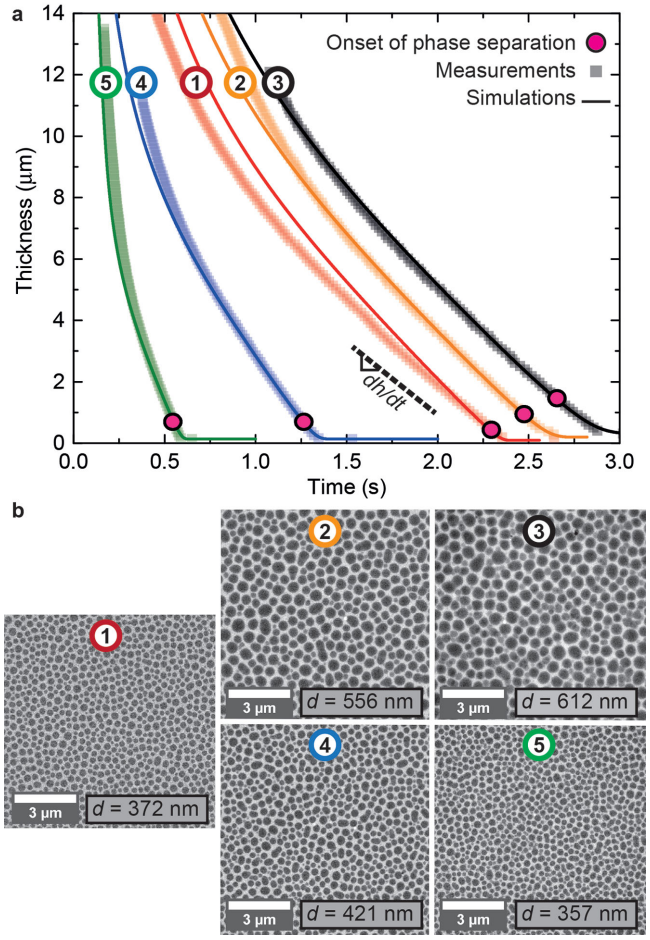

Figure 2. a) Drying curves and b) TEM images for five different films of PDPP5T:[70]PCBM spin coated from chloroform: 1) C_{pol} = 3 mg mL^{-1} and ω = 500 rpm; 2) C_{pol} = 6 mg mL^{-1} and ω = 500 rpm; 3) C_{pol} = 9 mg mL^{-1} and ω = 500 rpm; 4) C_{pol} = 6 mg mL^{-1} and ω = 1000 rpm, and 5) C_{pol} = 9 mg mL^{-1} and ω = 3000 rpm. The drying curves in panel (a) show both measurements (semitransparent squares) and the numerical model prediction (solid lines), as well as the onset of phase separation as measured by the onset of scattered light (pink circles). Measurements are translated along the time axis to coincide with the model at a thickness of 1 μm. The dashed line indicates how dh/dt is extracted. The scale bar in the TEM images is 3 μm. The inset in the TEM images shows the dominant length scale d obtained from the main peak in the Fourier-transformed images.

not influenced by the drying rate verifies our assumption of a uniform "bulk" concentration, because for higher drying rates surface-initiated phase separation would occur at a higher "bulk" solvent concentration. Also the fact that the [70]PCBM-rich droplets are surrounded by a skin layer of the matrix phase in cross-sectional TEM-images[9] indicates that the droplets originate in the bulk. Finally, this assumption is also verified by the fact that the drying model outlined in Section 2.2, which assumes a uniform solvent concentration, can accurately predict our drying curves. We note that we do not exclude the possibility of stratification or surface-initiated phase separation, but we have not seen any indication of significant effects of stratification.

2.4. Dominant Length Scale

It has been suggested[8,9] that length scales are determined by spin speed ω or the related drying rate, which is the slope in Figure 2a at the moment of phase separation (abbreviated as dh/dt). If this would be true, one would expect samples 1–3 in Figure 2 (three different ink concentrations spin coated at 500 rpm) to have a similar dominant length scale. This is not the case, because the dominant length scale has almost doubled from 372 nm to 612 nm. Moreover, samples 1, 4, and 5 would be expected to show widely different length scales where in fact they are remarkably similar: ranging from 357 to 422 nm. Thus, the initial ink concentration cannot be ignored. **Figure 3**a shows our large dataset, in which we studied three different initial concentrations at various spin speeds. It shows that the dependence of the dominant length scale on dh/dt (and thus ω) is only valid when considering a single ink concentration.

It was also suggested that length scales are determined by the final layer thickness h_{dry}.[10] Again, this is only true when looking at a single ink concentration as is shown in Figure 3b, or at a single spin speed.[10] However, Figure 3c shows very clearly that a scaling law can be found that relates the dominant length scale d for different concentrations and spin speeds to a normalized drying rate α, which is defined as the division of the drying rate (dh/dt) by the final thickness (h_{dry}). The physical origin of this normalized drying rate will be discussed below. Using this normalized drying rate, all concentrations coincide and form a line on a log-log plot, which fits Equation 3:

$$d \propto \alpha^b \text{ with } \alpha = \frac{\frac{dh}{dt}}{h_{dry}} \text{ and } b = -0.33 \pm 0.01 \quad (3)$$

A similar scaling can be found if dh/dt is not divided by the final thickness, but by the initial concentration of solids or the final thickness squared. We believe that our proposed normalized drying rate α is the most plausible, because α can be related to two possible "determinants" of the dominant length scale, which we will show in Section 2.7.

Equation 3 reveals that films with a similar thickness that have dried faster will have a smaller dominant length scale, because the exponent b is negative. Equation 3 also shows that when dried at the same rate, thicker films will have a larger dominant length scale.

2.5. Detailed Analysis of TEM Images

The TEM images of the spin coated PDPP5T:[70]PCBM films are investigated in more detail by image analysis to determine the midpoints and size of the droplets, which are then statistically analyzed. To remove noise from the TEM images (as in **Figure 4**a) a mean filter is applied, as explained in the Experimental Section. Then the images are binarized using global thresholding, after which small features are removed by opening and closing algorithms, as detailed in the Experimental Section. To avoid the "growing together" of separate droplets after binarization a watershed algorithm is applied. A typical resulting binary image is shown in Figure 4b. These methods

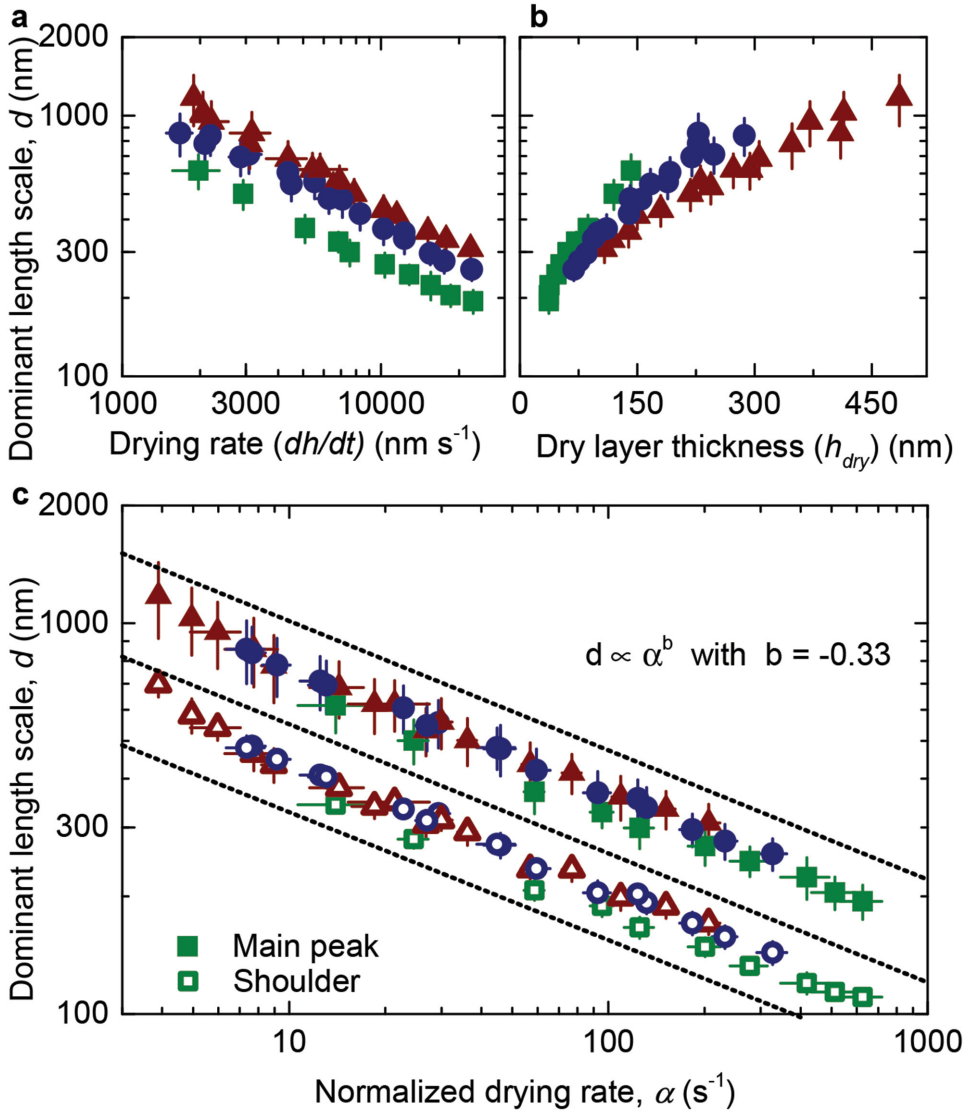

Figure 3. Relationship between the dominant length scale and normalized drying rate. Different initial polymer concentrations are indicated: green squares are 3 mg mL^{-1}, dark blue circles are 6 mg mL^{-1}, and dark red triangles are 9 mg mL^{-1}. Plots (a) and (b) show that a relation between the dominant length scale and drying rate respectively final thickness can be found for a single solution concentration. For different concentrations these relations are dissimilar. The horizontal axis in (c) is the normalized drying rate α, which is the drying rate divided by the final thickness. Then a scaling law is found which is valid for all concentrations. Solid symbols indicate the main peak position from the Fourier transform, while open symbols represent the location of the shoulder.[20]

are described in more detail in the Experimental Section. For each sample, the binarized images are analyzed in three ways: in Figure 4c a histogram of equivalent droplet radii (defined as $r = (A/\pi)^{1/2}$ where A is the area of the droplet) is shown; Figure 4d shows the nearest-neighbor distance distribution function $D(r)$. The pair correlation function $g(r)$, which describes the relative frequency of pairs of droplet centers with a distance of r to each other, is shown in Figure 4e. Finally, in Figure 4f all results are combined and compared with the results from FT. The first peak in $g(r)$ corresponds with the peak in the FT analysis. Furthermore, by plotting either $D(r) = 50\%$ or the average equivalent droplet radius versus the normalized drying rate, a similar scaling as in Equation 3 can be found. This strong correlation between these measures of length scales shows that the general use of the term "length scale" is valid. For example, the dominant length scale d is 2.9 ± 0.1 times larger than the average equivalent droplet radius. The small standard deviation shows that the discussion in this article is equally valid if dominant length scale was replaced by average equivalent droplet radius ($\overline{r}$). It is interesting that the histograms in Figure 4c do not show a significant bimodal distribution, even though there is a clear shoulder in the radially integrated FTs for these images.[20]

2.6. Other Material Combinations

To check if the scaling as a function of the normalized drying rate is specific for our system or more general, the same type

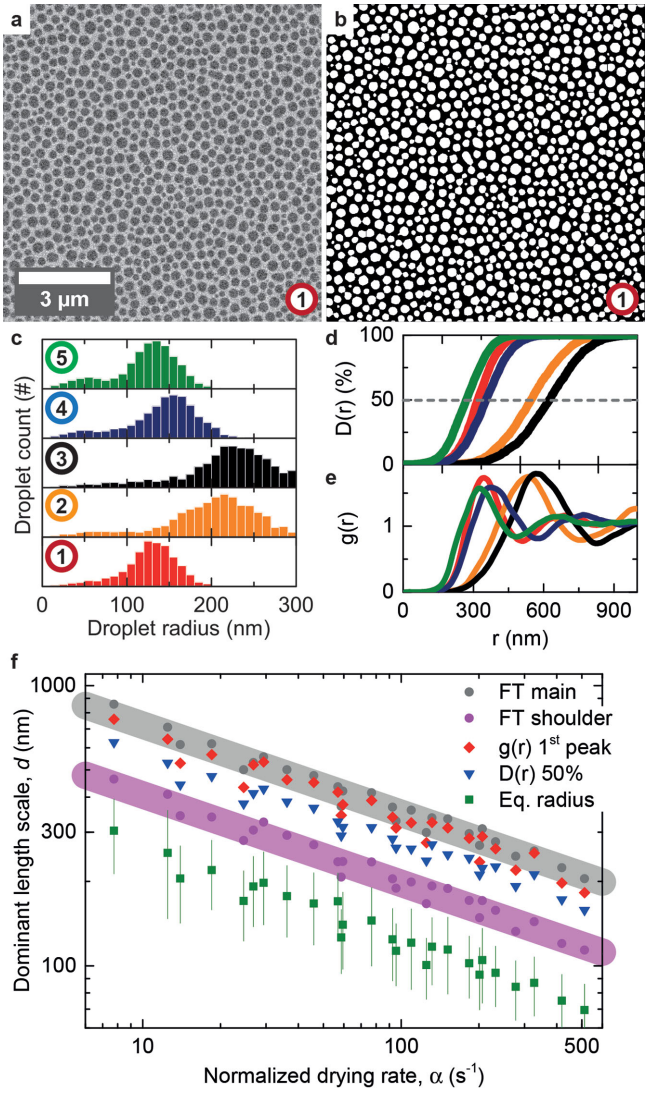

Figure 4. Image analysis. TEM images are analyzed in more detail using image analysis: in (a) a typical original TEM image is shown which is then binarized in (b). Histograms of droplet radii are shown in (c), where the colors and numbers correspond to Figure 2. Considering the midpoints of droplets, in (d) the probability of encountering a neighbor within a certain distance is shown: the nearest-neighbor distance distribution function $D(r)$. In (e) the pair correlation function $g(r)$ for this point pattern is shown. Finally, in (f) all analysis techniques are combined. The bands are used to highlight the data from the FTs which is shown in Figure 3 as well.

of measurements were performed for different material combinations. First, the influence of the ratio between PDPP5T and [70]PCBM was checked. For a 1:1 ratio the same scaling can be found. However, the 1:3 ratio seems to divide into separate scalings for each concentration, which was not expected. The origin of this is unknown but might be related to the fact that the used [70]PCBM concentration is close to the solubility limit. It might also be possible that, for this ratio, the droplet size is not limited by phase separation but by layer thickness. A hint for this effect is the linear relation between dry layer thickness and dominant length scale (Figure S6, Supporting Information), which is not found for lower [70]PCBM concentrations (Figure 3b). Secondly, a mixture of polystyrene (PS) and [70]PCBM was tested to check the influence of the polymer. Finally, a polystyrene:poly(methyl methacrylate) (PS:PMMA) system has been used to check the influence of [70]PCBM. All these samples show the expected scaling of the dominant length scale to the relation from Equation 3. All scaling plots can be found in the Supporting Information.

The results of fitting Equation 3 to each system are detailed in **Table 1**. It must be said that the number of data points for each fit is limited, which causes significant uncertainty. It is striking that, within the margin of error, the fit parameter b is the same for each system that contains [70]PCBM. However, there is a significantly stronger dependence of the dominant length scale on the normalized drying rate for the PS:PMMA system. Finally, the solvent content at the onset of a scattering signal should correspond to the concentration at which the system becomes unstable. It is interesting to compare this with (theoretical) phase diagrams. For example, the phase diagram given by Kouijzer et al.[9] predicts that the 1:2 system enters the unstable region below ~86% chloroform, which is close to the measured value. However, the measurement method and the limited number of samples limit the accuracy of these numbers for the other material combinations.

2.7. The Origin of the Dominant Length Scale Scaling

In the previous sections we have shown that the dominant length scale scales with the normalized drying rate α, which was defined as the division of the drying rate by the final thickness. Here we discuss the origin of this scaling parameter.

The dry-layer morphologies which are formed during spin coating originate from an initial structure formed by spinodal demixing that subsequently coarsens until the layer solidifies.[8b,9] Spinodal demixing and coarsening are driven by diffusion, induced by gradients in the chemical potential. We do not consider any flow-related mass transport in this discussion. Small length scales are expected for faster solvent evaporation both during the early stage spinodal demixing as well as during the subsequent late-stage coarsening. For the early stage spinodal demixing an increased evaporation rate allows the mixture to become more instabilized before demixing so that finer structures with larger interfacial areas can be formed. For the late-stage coarsening an increased evaporation rate reduces the time available for coarsening, which also leads to smaller length scales.

Based on in situ experiments, Toolan et al.[8b] propose that the dominant length scale is dictated by the rate of the quench, for which they use the rate of change of an effective interaction parameter. Theoretically, it is expected that length scales in early stage spinodal demixing originate from the rate of concentration change at the onset of phase separation. Both definitions of quench rate will lead to the derivation in Equation 4, but here the second approach is followed to show that the quench rate scales with our normalized drying rate α. The mean volume fraction of solid material ϕ_s is at any time given by the final thickness divided by the current thickness: $\phi_s = \frac{h_{dry}}{h[t]}$. Phase separation occurs when the system enters the spinodal region of the phase diagram, that is at a certain solid concentration $\phi_{spinodal}$. There the thickness

Table 1. Results from the scaling law for different material systems.

System	blend ratio	solvent	$\phi_{unstable}$ [a)] [%]	d [b)] [nm]	b [c)] [–]	R^2 [d)]
PDPP5T:[70]PCBM	1:1	chloroform	75 ± 6	241	0.28 ± 0.05	0.80
PDPP5T:[70]PCBM	1:2	chloroform	80 ± 3	355	0.33 ± 0.01	0.97
PDPP5T:[70]PCBM	1:3	chloroform	72 ± 6	490	0.33 ± 0.06	0.77
PS:[70]PCBM	1:2	chloroform	76 ± 4	548	0.35 ± 0.04	0.87
PS:[70]PCBM	1:2	o-xylene	71 ± 5	258[e)]	0.35 ± 0.04	0.89
PS:PMMA	1:1	chloroform	87 ± 4	1044	0.54 ± 0.07	0.82

[a)]The solvent content at the onset of a scattering signal; [b)]The dominant length scale d is calculated using the fitted pre-factor and the exponent b with $\alpha = 100$ in Equation 3. For chloroform-based systems $\alpha = 100$ is a representative normalized drying rate; [c)]Defined in Equation 3; [d)]The adjusted R^2 is indicative of the fit-quality for parameter b, closer to 1 is better; [e)]Note that for o-xylene $\alpha = 100$ will not be reached, and thus length scales in reality will be larger.

$h\left[t_{\text{spinodal}}\right] = h_{\text{dry}} / \phi_{\text{spinodal}}$. We express the quench rate $\mathrm{d}\phi_s / \mathrm{d}t$ at this moment in Equation 4:

$$\frac{\mathrm{d}\phi_s}{\mathrm{d}t} = \frac{\mathrm{d}\phi_s}{\mathrm{d}h}\frac{\mathrm{d}h}{\mathrm{d}t} = \frac{-h_{\text{dry}}}{h[t]^2}\frac{\mathrm{d}h}{\mathrm{d}t} = \frac{-h_{\text{dry}}}{\left(h_{\text{dry}} / \phi_{\text{spinodal}}\right)^2}\frac{\mathrm{d}h}{\mathrm{d}t} = \frac{-\phi_{\text{spinodal}}^2}{h_{\text{dry}}}\frac{\mathrm{d}h}{\mathrm{d}t} \propto \alpha \tag{4}$$

Thus, the existence of a scaling of dominant length scale to α could indicate a dependence of dominant length scale on the quench rate.

If length scales were to be determined solely by late-stage coarsening one would expect the dominant length scale to be related to the "time which is available for coarsening": $t_{\text{coarsening}}$. An estimate for $t_{\text{coarsening}}$ can be given as the time between initial phase separation and a totally dry layer as is shown in Equation 5, which is similar to α^{-1}, except for a constant:

$$t_{\text{coarsening}} \propto \frac{h\left[t_{\text{spinodal}}\right]}{\mathrm{d}h / \mathrm{d}t} = \frac{1}{\phi_{\text{spinodal}}}\frac{h_{\text{dry}}}{\mathrm{d}h / \mathrm{d}t} \propto \alpha^{-1} \tag{5}$$

Apart from the constant ϕ_{spinodal} the "time for coarsening" given by Equation 5 is actually the inverse of the "rate of concentration change" given by Equation 4. Thus, the existence of a scaling of dominant length scale to α could just as well indicate a dependence of dominant length scale on late-stage coarsening processes.

Because the scaling law for the dominant length scale found in Equation 3 can be related to either early stage processes via Equation 4 or late-stage processes via Equation 5 the existence of a scaling does not give any information about the main "determinant" of this dominant length scale. The fact that $b \approx -0.33$ for all systems that contain [70]PCBM might hint towards the importance of late-stage coarsening in the determination of the dominant length scale, because this b is very similar to the exponent which would be expected for Ostwald ripening.[9,16] However, length scales in early stage spinodal demixing and other coarsening mechanisms might play a role as well, which might be necessary to explain the larger b that has been found for the PS:PMMA system.

3. Conclusion

Using a combination of in situ techniques and numerical modeling we have analyzed the drying process of spin coated inks that undergo liquid–liquid phase separation. This knowledge is essential to understand the key parameter that controls length scales in phase-separated films, which can be analyzed only when completely dry. We found that the dominant length scale does not scale with the drying rate or with the final thickness; however, the division of drying rate by final film thickness results in a "normalized drying rate" for which a scaling of dominant length scale is found. The scaling is valid over two orders of magnitude and additionally verified for several material combinations. We have shown that this normalized drying rate can be related to two possible "determinants" of domains size: 1) the quench rate, which would determine length scales by the amplification of an initial length scale by spinodal decomposition (early stage), or 2) to the coarsening time, in which the growth of already existing domains can take place (late-stage, for example Ostwald ripening). The resulting dataset is important for further theoretical research to expand the understanding of phase separation; the discovered scaling factor should be reproduced by simulations. Understanding phase separation is essential for all organic electronic device fabrication, in which the optimization of the degree and dominant length scale of phase separation is crucial for device performance.

4. Experimental Section

Substrate Preparation: A 40 nm thick poly(ethylenedioxythiophene):poly(styrene sulfonate) (PEDOT:PSS, Heraeus Clevios P VP Al 4083) layer was spin coated on UV-ozone treated silicon substrates (Si-Mat, 525 µm thickness, 200 nm SiO_2 layer).

Solution Preparation: The diketopyrrolopyrrole-quinquethiophene polymer (PDPP5T, supplied by BASF, GSID4133–1) was mixed with [6,6]-phenyl-C_{71}-butyric acid methyl ester ([70]PCBM, Solenne, 90–95%) and dissolved in pure chloroform by overnight stirring at 65 °C. The results shown in the figures are based on a polymer concentration of 3, 6, or 9 mg mL^{-1} and the PDPP5T:[70]PCBM ratio was 1:2. All other rows in Table 1 are based on at least two solutions: both 3 and 9 mg mL^{-1} of the first indicated component is mixed with the indicated ratio of the second component. Polystyrene was supplied by Sigma-Aldrich (M_w = 280 kg mol^{-1}) and poly(methyl methacrylate) was supplied by Sigma-Aldrich (M_w = 350 kg mol^{-1}).

Spin Coating: Spin speeds between 6000 and 500 rpm were used to vary the drying rate and layer thickness. For even lower drying rates a two-step spin program was used, where the spin coater was set to spin for 0.3 seconds at 500 rpm and then slow down to spin speeds between 0 and 350 rpm. The spin coater acceleration was always 17 000 rpm s^{-1}. Dry film thicknesses were measured with a Veeco Dektak 150 profilometer.

Interference and Scattering: Initially a Melles-Griot 5 mW, 633 nm HeNe laser was used. For thicker films the absorption at this wavelength was too severe and thus for some series a 830 nm Newport LNQ830–150C laser diode was used, which was operated at 30 °C and 60 mA by a Newport model 505B laser diode driver. A biconvex lens was used to spread the laser beam to a spot of ≈3 mm radius, which effectively removes local disturbances by averaging a larger area. The specular reflected beam was incident on a diffuser to be able to filter out a slight wobble in the spinning disk. Behind the diffuser a Thor Labs SM1PD1A photodiode collected the light. The short-circuit current of the photodiode was amplified by a Stanford Research System Model SR570 current preamplifier operated in high-bandwidth mode. Off-specular scattered light was collected by a Hamamatsu S2281 photodiode under a ~45° angle and amplified by a second SR570. Both amplified signals were then measured as a voltage by a Keithley 2636A sourcemeter. A test-script protocol (TSP) script was used for simultaneous two-channel measurements. A time resolution between 0.5 to 2 ms was chosen, depending on the total drying time.

Thickness Calculation: The interference pattern was analyzed by an automatic peak and valley selection script in Wolfram Mathematica 9.0. The automatic selection was always checked manually. The thickness was backwards reconstructed from the interference signal and the dry layer thickness by repetitive addition of $\frac{\lambda}{4n\cos(\theta)}$ (≈100 nm) for each encountered peak or valley. Here, λ is the wavelength of the laser and θ is the angle of incidence of the laser on the substrate. The refractive index n is estimated using a weighted average based on the approximate volume fractions of all components.

TEM: Ultra-pure water was used to dissolve the PEDOT:PSS and float the films on 200 square mesh copper grids. A Tecnai G2 Sphera TEM (FEI) was operated at 200 kV. Magnifications as low as 550 × were used for the systems with the largest length scales, while for the smallest length scales a 5000× magnification was used.

FT Image Analysis: A 2D Fourier-transform was applied to at least five images per sample, using the ImagePeriodogram function in Wolfram Mathematica 9.0. These were radially integrated by taking the mean value of all pixels at the same distance from the center. The resulting 1D FTs were averaged for each sample. The *x*-axis was converted to real space, while the *y*-axis gives average pixel intensity $I(x)$. The main peak was selected automatically as the mean *x*-value of all points with $I(x) > 0.9 \times (I_{max} - I_{min})$, with the corresponding standard deviation. A reliable automatic shoulder position could only be obtained by finding the point with the smallest slope at distances lower than the main peak. This does not identify the actual shoulder position but is reliably and consistently related to its position. Both main peak and shoulder were always checked manually.

Mean Filter: Filtering is a smoothing method to suppress background noise in digital images. It is an important spadework before binarizing images. One possible method for filtering is the mean filter, which replaces every pixel value with the mean value of its value and the surrounding pixel values. More formally, let I be an image, where $I(i, j)$ denotes the pixel value at position (i, j). Every pixel value $I(i, j)$ at position (i, j) is changed according to the following rule:

$$I^{r}_{\text{mean}}(i,j) = \frac{\sum_{(k,l)\in U((i,j),r)} I(k,l)}{\#\left\{(k,l) \in U\left((i,j),r\right)\right\}}, \tag{6}$$

where $U((i, j), r)$ contains all positions within a distance r to position (i, j). In the present work, $r = 5$ leads to the best results. For more information, see for example Burger et al.[21]

Opening and Closing: Opening and closing are methods in digital image processing that remove noise in binary images. A binary image I is an image that consists only of two phases, foreground and background. We define $I(i, j) = 1$ for all foreground pixels and $I(i, j) = 0$ for all background pixels. Furthermore, let F be the set of foreground pixels, i.e., $F = \left\{(i,j) : I(i,j) = 1\right\}$ and $B = F^{c}$ its complement. First we consider a so-called erosion with a ball B^{x}_{r} with radius r around x,

$$(I \ominus B_r)(i,j) = \begin{cases} 1, \text{if } B^{x}_{r} \cap F, \\ 0, \text{otherwise.} \end{cases} \tag{7}$$

That is, the foreground F is shrunk in a certain way. The opposite operation, dilation, is defined as

$$(I \oplus B_r)(i,j) = \begin{cases} 1, \text{if } B^{x}_{r} \cap \mathrm{F} \neq \varnothing, \\ 0, \text{otherwise.} \end{cases} \tag{8}$$

That is, the foreground F grows slightly. Note that dilating the foreground is equivalent to eroding the background. Opening and closing are then defined as first eroding, and then dilating again, and vice versa, respectively. That is,

$$\mathrm{op}_{r}(F) = (I \ominus B_r) \oplus B_r \tag{9}$$

and

$$\mathrm{cl}_{r}(F) = (I \oplus B_r) \ominus B_r \tag{10}$$

As small structures disappear completely when eroding the image, they do not grow again when dilating. Thus, opening removes small structures in the foreground, and closing small structures in the background. For further information, see for example Soille.[22]

Watershed Algorithm: The watershed algorithm is a tool for segmentation of image data. It can be used to detect objects in an image that are grown together, and split them. Given a binary image displaying a system of (possibly overlapping) particles (interpreted as foreground), first the maxima of the distance transformations from particles to background are computed. The distance transformation assigns every pixel belonging to the foreground its minimum distance to the background. Given the maxima of the distance transformation, they are all dilated uniformly. If two of those dilating circles hit each other, the corresponding particle is split on this position. The circles grow until they completely cover the corresponding particle. In this work, this procedure is performed using the software Fiji.[23]

Pair Correlation Function: When statistically analyzing a point pattern $\{p_i\}$, an important characteristic is the pair correlation function $g : [0,\infty) \to [0,\infty)$, where, $g(r)$ describes the relative frequency of point pairs (p_i, p_j) with a distance of r to each other. Interesting is especially the location of peaks in this function, that is, the distance of point pairs that occurs with largest frequency. For a more formal definition of the pair correlation function, see for example Illian et al.[24]

Nearest-Neighbor Distance Distribution Function: The nearest-neighbor distance distribution function for a point pattern $\{p_i\}$ is defined as follows. For each point p_i of the point pattern we consider the distance d_i to the point p_j that is closer to p_i than any other point in $\{p_i\}$, that is,

$$d_i = \min_{j \neq 1} \left| p_i - p_j \right| \tag{11}$$

The distribution function of those minimum distances d_i is called nearest-neighbor distance distribution function $D : (0,\infty] \to [0,1]$. For more information, see for example Illian et al.[24]

Supporting Information

Supporting Information is available from the Wiley Online Library or from the author.

Acknowledgements

The authors would like to thank Charley Schaefer (Eindhoven University of Technology) and Jasper Michels (Holst Centre) for fruitful discussions about the theoretical background of phase separation, and Tamara Eggenhuisen (Holst Centre) for viscosity measurements. This research forms part of the research programme of the Dutch Polymer Institute (DPI), project #734. The work of was further supported by the Deutsche Forschungsgemeinschaft under Priority Programme 1355 'Elementary Processes of Organic Photovoltaics' and is part of the Solliance OPV program and has received funding from the Ministry of Education, Culture and Science (Gravity 382 program 024.001.035).

Received: September 28, 2014
Revised: November 3, 2014
Published online: December 1, 2014

[1] a) B. W. D'Andrade, S. R. Forrest, *Adv. Mater.* **2004**, *16*, 1585; b) N. Rehmann, D. Hertel, K. Meerholz, H. Becker, S. Heun, *Appl. Phys. Lett.* **2007**, *91*, 103507.

[2] a) S. E. Shaheen, C. J. Brabec, N. S. Sariciftci, *Appl. Phys. Lett.* **2001**, *78*, 841; b) H. Hoppe, T. Glatzel, M. Niggemann, W. Schwinger, F. Schaeffler, A. Hinsch, M. Ch. Lux-Steiner, N. S. Sariciftci, *Thin Solid Films* **2006**, *511–512*, 587; c) C. J. Brabec, S. Gowrisanker, J. J. M. Halls, D. Laird, S. Jia, S. P. Williams, *Adv. Mater.* **2010**, *22*, 3839; d) L. Dou, J. You, Z. Hong, Z. Xu, G. Li, R. A. Street, Y. Yang, *Adv. Mater.* **2013**, *25*, 6642.

[3] a) K. Asadi, D. M. de Leeuw, B. de Boer, P. W. M. Blom, *Nat. Mat.* **2008**, *7*, 547; b) V. Khikhlovskyi, R. Wang, A. J. J. M. van Breemen, G. H. Gelinck, R. A. J. Janssen, M. Kemerink, *J. Phys. Chem. C.* **2014**, *118*, 3305.

[4] P. J. Dowding, R. Atkin, B. Vincent, P. Bouillot, *Langmuir* **2004**, *20*, 11374.

[5] a) D. R. Lloyd, S. S. Kim, K. E. Kinzer, *J. Membr. Sci.* **1991**, *64*, 1; b) K. S. McGuire, A. Laxminarayan, D. R. Lloyd, *Polymer* **1995**, *36*, 4951.

[6] J.-C. Loudet, P. Barols, P. Poulin, *Nature* **2000**, *407*, 611.

[7] a) S. Z. D. Cheng, *Phase Transitions in Polymers: The Role of Metastable States*, Elsevier, Amsterdam, The Netherlands **2008**, p. 45; b) K. Binder, *J. Chem. Phys.* **1983**, *79*, 6387; c) T. Izumitani, T. Hashimoto, *J. Chem. Phys.* **1985**, *83*, 3694; d) P. D. Graham, A. J. McHugh, *Macromolecules* **1998**, *31*, 2565; e) V. Sofonea, K. R. Mecke, *Eur. Phys. J. B.* **1999**, *8*, 99.

[8] a) K. Dalnoki-Veress, J. A. Forrest, J. R. Stevens, J. R. Dutcher, *Physica A* **1997**, *239*, 87; b) D. T. W. Toolan, E. ul Haq, A. Dunbar, S. Ebbens, N. Clarke, P. D. Topham, J. R. Howse, *J. Polym. Sci., Part B: Polym. Phys.* **2013**, *51*, 875.

[9] S. Kouijzer, J. J. Michels, M. v. d. Berg, V. S. Gevaerts, M. Turbiez, M. M. Wienk, R. A. J. Janssen, *J. Am. Chem. Soc.* **2013**, *135*, 12057.

[10] E. L. Williams, S. Gorelik, I. Y. Phang, M. Bosman, C. Vijila, G. S. Subramanian, P. Sonar, J. Hobley, S. P. Singh, H. Matsuzaki, A. Furube, R. Katoh, *RSC Adv.* **2013**, *3*, 20113.

[11] S. Nilsson, A. Bernasik, A. Budkowski, E. Moons, *Macromolecules* **2007**, *40*, 8291.

[12] K. Maturová, S. S. van Bavel, M. M. Wienk, R. A. J. Janssen, M. Kemerink, *Nano Lett.* **2009**, *9*, 3032.

[13] D. Bartesaghi, M. Turbiez, L. J. A. Koster, *Org. Electron.* **2014**, *15*, 3191.

[14] D. Bartesaghi, L. J. A. Koster, *Adv. Funct. Mater.* **2014**, doi: 10.1002/adfm.201402260.

[15] F. Liu, C. Wang, J. K. Baral, L. Zhang, J. J. Watkins, A. L. Briseno, T. P. Russell, *J. Am. Chem. Soc.* **2013**, *135*, 19248.

[16] A. Baldan, *J. Mater. Sci.* **2002**, *37*, 2171.

[17] a) F. Horowitz, E. J. C. Dawnay, M. A. Fardad, M. Green, E. M. Yeatman, *J. Nonlinear Opt. Phys. Mater.* **1997**, *6*, 1; b) D. Birnie, *Phys. Fluids* **1997**, *9*, 870; c) P. C. Jukes, S. Y. Heriot, J. S. Sharp, R. A. L. Jones, *Macromolecules* **2005**, *38*, 2030; d) S. Y. Heriot, R. A. L. Jones, *Nat. Mater.* **2005**, *4*, 782; e) P. Mokarian-Tabari, M. Geoghegan, J. R. Howse, S. Y. Heriot, R. L. Thompson, R. A. L. Jones, *Eur. Phys. J. E* **2010**, *33*, 283; f) S. Ebbens, R. Hodgkinson, A. J. Parnell, A. Dunbar, S. J. Martin, P. D. Topham, N. Clarke, J. R. Howse, *ACS Nano*, **2011**, *5*, 5124; g) D. T. W. Toolan, J. R. Howse, *J. Mater. Chem. C* **2013**, *1*, 603; h) D. T. W. Toolan, A. J. Parnell, P. D. Topham, J. R. Howse, *J. Mater. Chem. A*, **2013**, *1*, 3587.

[18] A. G. Emslie, F. T. Bonner, L. G. Peck, *J. Appl. Phys.* **1958**, *29*, 858.

[19] D. E. Bornside, C. W. Macosko, L. E. Scriven, *J. Electrochem. Soc.* **1991**, *138*, 317.

[20] W. Burger, M. J. Burge, *Digital Image Processing: An Algorithmic Introduction Using Java*, Springer, New York **2010**.

[21] P. Soille, *Morphological Image Analysis: Principles and Applications*, Springer, Berlin **2003**.

[22] J. Schindelin, I. Arganda-Carreras, E. Frise, V. Kaynig, M. Longair, T. Pietzsch, S. Preibisch, C. Rueden, S. Saalfeld, B. Schmid, B. S. Tinevez, D. J. White, V. Hartenstein, K. Eliceiri, P. Tomancak, A. Cardona, *Nat. Methods* **2012**, *9*, 676.

[23] J. Illian, A. Penttinen, H. Stoyan, D. Stoyan, *Statistical Analysis and Modelling of Spatial Point Patterns*, J. Wiley & Sons, Chichester **2008**.

[24] In Figure 3c not only the dominant length scale is shown, but also the shoulder found in the Fourier transforms as indicated in Figure 1. The position of the shoulder is mathematically found by detecting the smallest slope in the radially integrated Fourier transform. This does not detect the actual peak position which underlies the shoulder but is a representative distance which is more strictly defined. The scaling in Equation (3), as found for the main FT peak, is also valid for the shoulder. The origin of the shoulder is presently unknown and presented as an experimental observation.